Earth and Planetary Science Letters 333–334 (2012) 157–164

Contents lists available at SciVerse ScienceDirect

Earth and Planetary Science Letters

journal homepage: www.elsevier.com/locate/epsl

Response of forearc crustal faults to the megathrust earthquake cycle: InSAR evidence from Mejillones Peninsula, Northern Chile

M. Shirzaei [a,b,*], R. Bürgmann [a], O. Oncken [b], T.R. Walter [b], P. Victor [b], O. Ewiak [b]

[a] Department of Earth and Planetary Science, University of California, Berkeley, CA, USA
[b] Helmholtz Centre Potsdam, GFZ German Research Center for Geosciences, Potsdam, Germany

ARTICLE INFO

Article history:
Received 5 February 2012
Received in revised form
31 March 2012
Accepted 5 April 2012
Editor: P. Shearer

Keywords:
megathrust earthquake cycle
Tocopilla earthquake
InSAR and modeling
crustal fault creep

ABSTRACT

We report on a rare example of aseismic response of a creeping fault to the earthquake cycle of a nearby megathrust. Interferometric synthetic aperture radar (InSAR) is used to detect and analyze shallow creep of two crustal faults at Mejillones Peninsula, Northern Chile, located in the hanging wall of the 2007 Mw 7.7 Tocopilla subduction earthquake. We generate two independent time series of surface deformation spanning ~3.5 yr of late interseismic and ~1.5 yr early postseismic deformation associated with this event. The analysis reveals creep on the Mejillones fault as well as on a previously unmapped fault to the west of the Mejillones fault. The InSAR deformation maps and distributed slip models obtained from the data reveal that fault creep reversed between the interseismic and postseismic periods. Given the regional stress field perturbations due to interseismic and coseismic deformation, we argue that the observed shallow creep and its slip reversal are directly linked to the megathrust seismic cycle. Moreover, from similar eastward dips but opposite slip directions of the two faults, we infer that fault strength must be very low and that the kinematics is controlled by crustal flexure associated with the seismic cycle on the underlying megathrust.

1. Introduction

In subduction zones, the state of stress is highly time-dependent, linked to the seismic cycle of great megathrust earthquakes. The static coseismic deformation field and years to decades of postseismic deformation transients affect the state of stress over wide regions (e.g. Wang et al., 2007). Stress changes are particularly large on crustal faults in the hanging wall immediately landward of subduction zone earthquakes (Lin and Stein, 2004). For instance the 1995 Mw 8.0 Antofagasta earthquake in northern Chile resulted in a wide zone of E–W extension in the coastal region that reduced interseismic loading on crustal faults (Delouis et al., 1998). Moreover, stress changes from recent megathrust ruptures in Chile and Japan have triggered multiple normal faulting earthquakes in the overriding plates (Kato et al., 2011; Ryder et al., 2012).

Frictionally weak faults that slip aseismically, i.e. creeping faults (Collettini et al., 2009), may change their rate and/or orientation of slip in response to external stress changes. The response of a creeping fault to regional stress perturbation was documented along the shallowly creeping Hayward fault, which experienced a reduction and even partial reversal of fault creep along its southern ~40 km following the 1989 Mw 6.9 Loma Prieta earthquake (Lienkaemper et al., 1997, 2012). A temporary reversal of surface creep was also observed near Parkfield on the creeping section of the San Andreas fault following the 1983 Mw 6.7 Coalinga earthquake (Simpson et al., 1988a; Toda and Stein, 2002). Here we explore slip on two creeping faults in northern Chile in the years before and after a large megathrust earthquake, in 2007.

Several large earthquakes have ruptured over 1000 km of the Chile subduction zone, since 1877 (Fig. 1). The 2007 Mw 7.7 Tocopilla earthquake that occurred near Mejillones Peninsula, where Quaternary extension and strike slip faulting has been documented (e.g. Delouis et al., 1998), provides an opportunity to investigate the response of crustal faults to a megathrust earthquake using synthetic aperture radar interferometry (InSAR) imaging geodesy. High resolution maps of the late interseismic (interseismic, henceforth), coseismic and early postseismic (postseismic, henceforth) surface deformation associated with this event are obtained by interferometric processing of SAR acquisitions of the Envisat radar satellite operated by the European Space Agency.

Mejillones Peninsula is located near an apparent barrier for along-arc rupture propagation of megathrust earthquakes, including the 1995 Mw 8.0 Antofagasta, 2007 Mw 7.7 Tocopilla, and the 1877 Mw 8.5 Iquique earthquakes (Loveless et al., 2010; Victor

* Corresponding author at: Department of Earth and Planetary Science, University of California, Berkeley, CA, USA.
E-mail address: shirzaei@berkeley.edu (M. Shirzaei).

0012-821X/$ - see front matter © 2012 Elsevier B.V. All rights reserved.
http://dx.doi.org/10.1016/j.epsl.2012.04.001

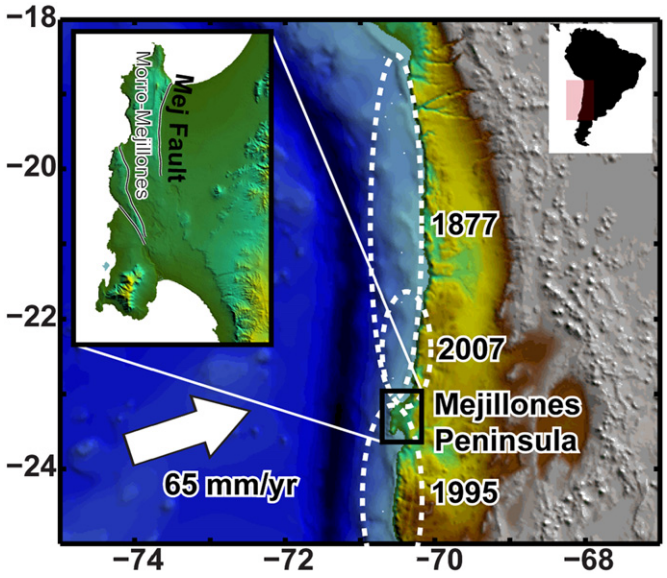

Fig. 1. Study area. The approximate rupture area of the historical earthquakes is plotted. The box with thick black line shows the Mejillones Peninsula. Inset show a closer view of the Mejillones Peninsula as well as location of the Mej (Mejillones) fault.

et al., 2011). In the north of the Peninsula, the Morro Mejillones range (Fig. 1) is bounded to the east by the eastward dipping Mejillones (Mej) normal fault (Armijo and Thiele, 1990; Delouis et al., 1998).

Here we focus on detecting and characterizing shallow fault slip on Mejillones Peninsula over a 5-yr period spanning the 2007 Tocopilla earthquake. To this aim, we apply InSAR and investigate deformation during two distinct periods of earthquake cycle deformation, i.e., late interseismic and early postseismic deformation of the Tocopilla earthquake. Three sets of SAR data acquired by the Envisat radar satellite over the northern part of Mejillones Peninsula are processed. Four interferograms, spanning the time of the earthquake and as much as 6 and 3 months of the preseismic or postseismic deformation are used to find evidence of shallow faulting directly associated with the coseismic rupture. To characterize deformation before and after the earthquake, 26 and 11 SAR images, which span periods of 2003/1/4–2007/10/20 and 2007/11/24–2008/12/13, respectively, are used. Interferometric processing of these data sets provides us with a spatio-temporal map of the deformation field on Mejillones Peninsula for the interseismic, coseismic and postseismic periods of Tocopilla earthquake. These deformation maps together with dislocation modeling provide unique information about the dynamics of creeping faults at Mejillones Peninsula.

2. Methods

2.1. InSAR time series analysis

To generate a time series of the surface deformation field for both interseismic and postseismic episodes we employ a multiple-master SAR interferometry approach following earlier works (e.g. Berardino et al., 2002). Given 26 and 11 SAR scenes acquired before and after the 2007 earthquake, we generated 113 and 32 interferograms, respectively, with orbital and temporal baselines smaller than 400 m and 2 yr (see Supplementary Fig. S1 in the Appendix for baseline plots of these data sets). The pixel size is 20 m × 20 m equivalent to a multi-looking factor of 1 × 5 along range and azimuth, respectively. The geometrical phase is estimated and subtracted using satellite precise ephemeris data and a reference SRTM digital elevation model of 90 m resolution (Massonnet et al., 1993; Franceschetti and Lanari, 1999). To obtain an unambiguous phase observation from modulo 2π phase change measured in each interferogram, we use a 2D phase unwrapping operator (Chen and Zebker, 2001) and apply it to high quality pixels in the image (Costantini and Rosen, 1999). The algorithm for identifying high quality pixels is based on maps of coherence following earlier works (Berardino et al., 2002). The effect of satellite orbital error in each unwrapped interferogram is also reduced following the method proposed by Shirzaei and Walter (2011). This error is estimated as a best fitting plane (i.e. ramp) to the long-wavelengths components of each unwrapped interferogram using robust regression. Then, each data set is inverted using a linear unbiased estimation approach (Bjerhammar, 1973) to generate two separate time series of the inter- and postseismic displacement fields. High-pass filtering in time and low-pass filtering in space is applied to identify the atmospheric delay to be subtracted from each interferograms (Ferretti et al., 2001). The line-of-sight (LOS) velocity of each pixel is estimated as the slope of a best fitting line to the displacement time series using a robust regression approach (O'leary, 1990). The robust regression includes the advantages of L_1-norm minimization approaches and thus is able to suppress the negative impact of outliers and to obtain a reliable velocity field (O'leary, 1990).

2.2. Uniform slip inversion

For uniform slip inversion we simulated the fault planes using rectangular dislocations in an elastic half-space (Okada, 1985). The unknowns for each dislocation source include the width, depth, dip, and the model fault slip. The rake is fixed to obtain only dip slip and the location and length are constrained, within a reasonable range, using the surface trace of the faults. Apart from slip, the other fault parameters have nonlinear relations to the displacement field observed at the surface. Therefore, a nonlinear optimization approach should be implemented to solve for the dislocation source parameters. Here, we adapt Genetic Algorithms (GA) in an iterated manner (Shirzaei and Walter, 2009). This approach allows for estimating unknowns, which have fully nonlinear functional relation to the observations, as well as their associated uncertainty. GA uses several operators to avoid local minima and to reliably obtain the optimum values. For more details on GA and parameter initialization refer to Shirzaei and Walter (2009).

2.3. Distributed slip inversion

Following the determination of the optimal fault geometry in the previous step, to estimate the distribution of slip on the fault surface involves a linear inverse problem; therefore, a linear least square inversion approach is suitable (Stark and Parker, 1995). To this aim, the fault planes found in the geometry inversion are expanded laterally and along dip, subdivided into triangular elements (Meade, 2007) and a smoothed distributed slip model across the discretized faults is obtained.

To reduce the roughness of the slip on the fault plane and avoid unrealistic stress changes, we minimize the second-order derivative of the fault slip (e.g. Segall and Harris, 1987). Trade-off curves are used to select a smoothing factor that provides a balance between roughness and model fit to surface deformation data (see Supplementary Fig. S4 in the Appendix). The optimum smoothing factor is obtained at the location of maximum curvature of the trade-off curve (Tikhonov and Arsenin, 1977).

3. Observations

3.1. InSAR deformation data

Fig. 2a and b shows the LOS velocity (incidence angle=23°, heading angle=188°) obtained for the interseismic and postseismic periods, respectively. Positive velocities (red color) indicate movement toward the satellite relative to a reference point located to the east of the Morro Mejillones range (see also Supplementary Fig. S5 in the Appendix for examples of InSAR deformation time series). The central part of the range is characterized by negative and positive velocities relative to surrounding areas for the interseismic and postseismic episodes, respectively. This indicates that the sense of fault slip responsible for the localized deformation differed between the two observation periods separated by the large earthquake.

The area of maximum displacement at the center of the map is bounded on the east by the Mej fault. In addition, another area of high displacement gradient is observed to the west that coincides with a topographic scarp, which was not previously mapped as an active fault. The InSAR observations suggest that an unmapped active fault that is aseismically slipping at shallow depths is located along this scarp. This observation is also supported by new field evidence of recently formed cracks along the scarp (see Section 3.2). This supports our finding that the scarp represents the surface trace of an active fault, which we refer to here as the Morro fault. The surface traces of the Mej and Morro faults are well delineated in the two LOS velocity maps showing steep gradients in nearly identical locations for both episodes (Fig. 2a and b).

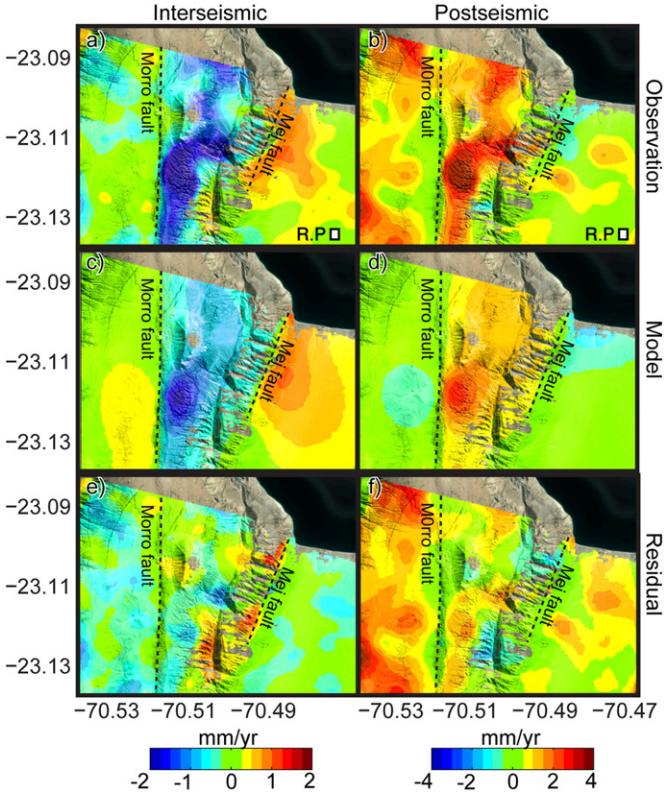

Fig. 2. Observation and model result for surface displacements during interseismic and postseismic periods. (a, b) Observed LOS velocity (incidence angle=23°, heading angle=188°), (c, d) predicted range change from dislocation model obtained in the distributed slip inversion, and (e, f) residuals (observed–modeled). The surface trace of the fault planes obtained from uniform slip inversion is marked by dashed line in panels c and d. (R.P=reference zero displacement point for InSAR time series). (For interpretation of the references to color in this figure legend, the reader is referred to the web version of this article.)

3.2. Field evidence for active faulting on Mejillones Peninsula

The long-term geological record shows that major faults on Mejillones Peninsula record mainly normal slip on generally N–S striking fault planes dipping to the east (Armijo and Thiele, 1990; Gonzalez et al., 2003; Allmendinger and Gonzalez, 2010). Despite ongoing extension at the surface, the Peninsula has been continuously uplifted since the Miocene (Armijo and Thiele, 1990; Delouis et al., 1998; Marquardt et al., 2005), due to bending of the subduction hanging-wall. The Morro fault is another fault that has now been detected by using InSAR in this study, located to the west of the Mej fault and the Morro Mejillones range (Figs. 2 and 3a and b). Field evidence shows that this fault is highly active and displaces granitic basement above much younger, weakly-consolidated terrestrial sediments overlying marine terraces of Pleistocene age (Fig. 3c–f). At the surface, the outcropping fault zone is almost vertical in the central part of the fault (Fig. 3a). Towards the north the fault plane clearly dips to the east with an average angle of about 75° as evidenced from a fault propagation fold above a blind, reverse-slip strand of the Morro fault (Fig. 3d and e). This easterly dip direction most likely continues along the central and southern parts of the fault at greater depth, because the basement rock shows a widely spaced foliation dipping to the east with an average dip of 70°, which is most likely an inherited fabric reactivated by active faulting. This recent reactivation is documented by numerous scarp-parallel open cracks that were mapped 3 yr after the earthquake (Fig. 3e). Cracking is abundant and concentrates directly along the scarp. Cracks also crosscut the youngest alluvial fans at the base of the scarps and even the most recent erosional streambeds. Most cracks have a length of several meters up to few tens of meters. The opening width usually ranges between 5 and 30 mm. Additional evidence for recent reactivation of the Morro fault and a high displacement rate in the central segment of the fault can be derived from the over steepened facets of the hanging wall, fresh appearance of rockfall material at the base of the scarp and alluvial fan surfaces not covered by desert varnish (Fig. 3f). Such young facets or rockfalls are not described for any other fault at Mejillones Peninsula or along the Atacama fault system thus pointing to a higher than average displacement rate. These observations document the Morro fault with a dominant reverse sense of hangingwall motion above an east-dipping fault, thus creating a scarp of up to 60 m that offsets the unconsolidated terrestrial sediments.

In contrast to the Morro Fault, the Mej Fault shows a dominant normal sense of motion on an east dipping fault plane well described by Armijo and Thiele (1990) and Gonzalez et al. (2003). Recent offsets in alluvial fan sediments are at maximum 14 m high and there are no oversteepened basement outcrops and young rockfall deposits.

4. Model results

During the initial geometry inversion using GA, we fix the coordinates of the end points of the two fault planes at the surface that are well known based on deformation data. Moreover, due to the north–south orientation of the Morro and Mej faults and the polar orbiting satellite track we are not able to resolve the rake angle uniquely. Thus we constrain it to accumulate only dip–parallel slip, while the other source parameters (dip, width, and magnitude of the slip vector) are treated as free unknowns. We perform two independent inversions for the interseismic and postseismic data sets. The optimized parameters of the rectangular dislocation sources as well as the associated 95% confidence intervals are provided in Table 1. The interseismic and postseismic uniform slip models reproduce the observations with a

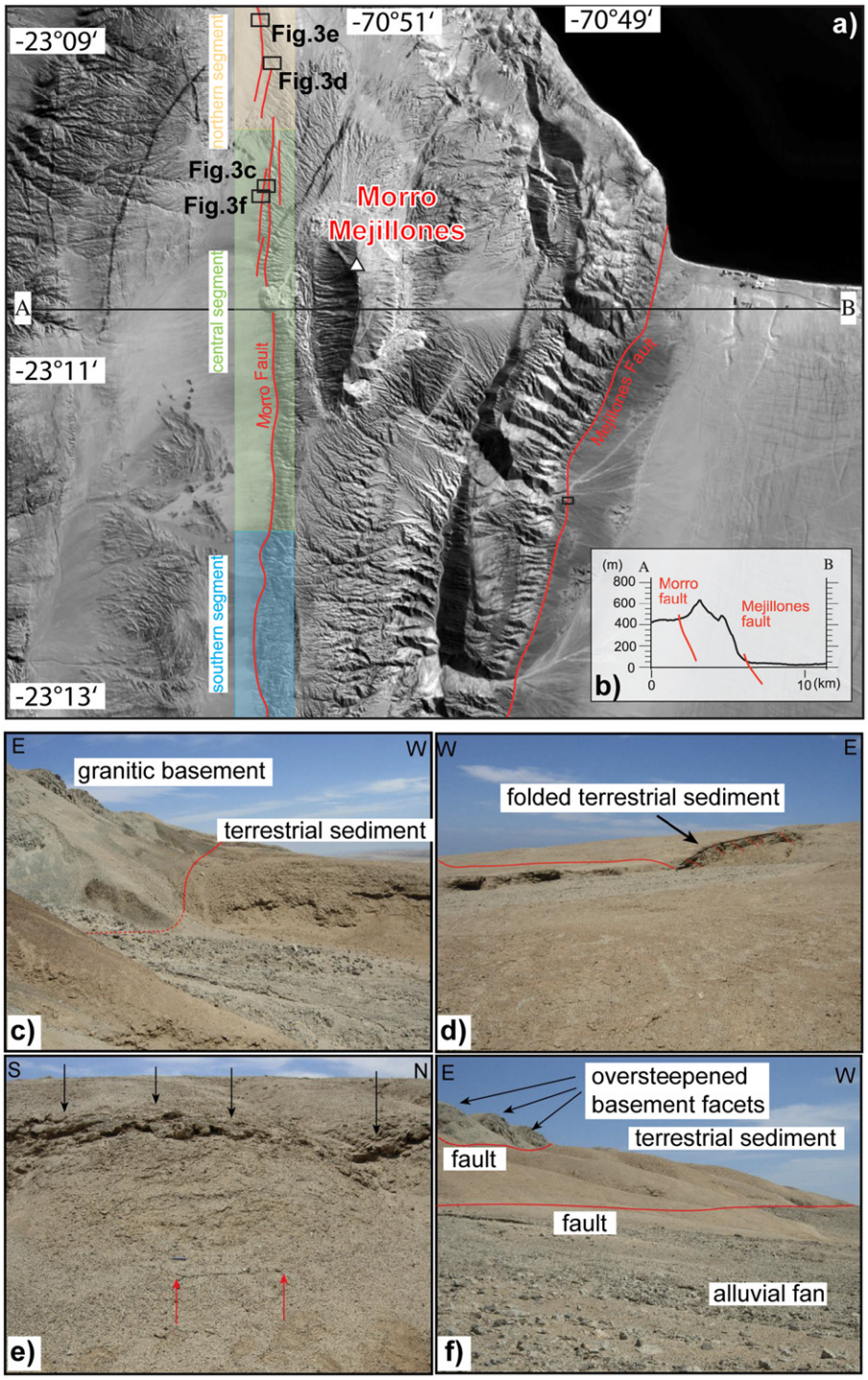

Fig. 3. Field evidence. (a) Location of the Morro and Mejillones faults to the west and east of the Morro-Mejillones range. (b) AB cross-section (a) showing the location and orientations of the Morro and Mej faults. (c–f) Photographs of the selected sites (a) and their associated interpretations providing evidence in support of an eastward dipping Morro fault.

standard deviation of 0.6 mm/yr and 0.9 mm/yr, respectively. Interestingly, the obtained dips and widths of the creeping portions of the Morro and Mej faults are very similar for interseismic and postseismic dislocation models. This implies that the fault geometries are solved reliably and the same faults are responsible for both episodes of activity, albeit with different kinematics.

The optimization favors steep eastward dips of both the Mej and Morro faults, consistent with field evidence, which slip in opposite directions during the interseismic and postseismic time periods. Since most major faults have normal kinematics in this part of the forearc system, we also tested the possibility of a west dipping Morro fault, under the assumption of it also being a normal fault. To this end, we perform another uniform slip inversion by constraining the Morro fault to dip westward between 40° and 75° with a minimum width of 2 km. The result of this modeling is shown in Supplementary Table S2 and Supplementary Fig. S3 in the Appendix. Clearly, a west-dipping

Morro fault is not able to reproduce the data. Such a model produces substantial localized deformation to the west, which is not observed. Thus we are confident that a model in which both faults dip to the east is required to explain the deformation data and field observations.

To estimate the distribution of slip on the Morro and Mej faults, we use the average dip obtained in the interseismic and postseismic inversions, extend the surfaces of the Morro and Mej faults by 20% laterally and down-dip, and subsequently subdivide them into 306 and 144 triangular elements, respectively. The average dimension of the dislocation triangles is 400 m. We impose a zero-slip constraint at the down-dip edge of the faults, where our data does not provide enough resolution. Fig. 2c and d presents the model predicted LOS velocity fields derived from the linear slip inversion with smoothing constraints and Fig. 2e and f shows the associated residuals (observed–modeled). The standard deviations of the residuals for the interseismic and postseismic periods are 0.3 mm/yr and 0.7 mm/yr, respectively. In the west of the postseismic residual map (Fig. 2f) there is an area characterized by red color, which is not removed by our model. This is due to a strong atmospheric delay in some of the generated interferograms that locally influences the estimated LOS velocity. One could remove the noisy acquisitions from the data set before the time series analysis. However, due to the small number of the SAR images acquired during the postseismic period, and because the atmospheric signal does not affect the area of interest, we decided to keep all interferograms to obtain a more precise LOS velocity over the Morro and Mej faults.

Fig. 4 and Supplementary Table S3 in the Appendix present the modeled slip on the Morro and Mej fault planes. The red and blue colors indicate reverse and normal faulting, respectively. For the interseismic period we find that the Morro fault is characterized by normal slip, while the result for the Mej fault indicates thrust motion. In contrast, during the postseismic episode the sense of motion is reversed on the Morro and Mej faults, showing thrust faulting and normal faulting, respectively. Most of the resolved slip is placed between 0.5 and 2.5 km depth. To the north, where the faults are under the water, additional slip is possible, but we cannot constrain it due to lack of data.

To evaluate if there was triggered slip on the Morro and Mej faults during the coseismic period, we generated a stack of four interferograms with orbital baseline shorter than 200 m spanning the coseismic deformation of the Tocopilla event (see Table S1). Following the sparse phase unwrapping we apply conventional data stacking (see e.g. Fialko, 2006) to improve the signal-to-noise ratio of the coseismic deformation map (see Supplementary Fig. S2a in the Appendix). After removing the broad signals due to the coseismic displacement, the residual LOS deformation shows a pattern similar to the postseismic deformation with two reversal points at the location of the Morro and Mej faults (see Supplementary Fig. S2b in the Appendix). This indicates that these two faults may have experienced a small amount of slip (~2–3 mm) during or shortly after the Tocopilla earthquake.

Table 1
The optimum parameters and associated 95% confidence intervals for the fault planes obtained in the uniform slip inversion of the interseismic and postseismic creep assuming pure dip slip. The coordinates of the start and end points of the Morro fault are given in UTM projection system (zone 19s) as (344.5 km, 7440.0 km) and (344.2 km, 7446.3 km) and for Mej fault are (346.6 km, 7442.9 km) and (347.8 km, 7445 km), respectively. Positive/negative dip slip indicates reverse/normal fault creep.

Period	Fault name	Dip slip (mm/yr)	Width (km)	Dip (deg.)
Interseismic	Morro	-1.9 ± 0.4	3.7 ± 0.6	53 ± 5
	Mej	$+1.6 \pm 0.3$	3.8 ± 1.2	73 ± 8
Postseismic	Morro	$+3 \pm 0.4$	3.8 ± 0.3	50 ± 4
	Mej	-1.7 ± 0.6	3.9 ± 1.5	54 ± 11

5. Discussion

The key observation of our analysis is the contemporaneous slip of two nearby, similarly oriented and possibly geometrically coupled faults in the forearc that exhibit opposing kinematics and that jointly reverse their slip direction following the Tocopilla megathrust earthquake on the underlying plate interface. This result seems to require very special stress and/or strength conditions. Fault creep appears to have been influenced by the perturbations of the stress field (Marone, 1998) resulting from the Tocopilla earthquake. Therefore, we explore whether the shear and normal stress imparted by the interseismic coupling and the coseismic rupture can explain the observed reversal in the sense of creep on the two faults.

To this end, we examine the induced interseismic and coseismic shear and normal stress (King et al., 1994) on two separate east-dipping faults located at the position of Mej and Morro faults with dip of 55° (i.e. the average dip of Mej and Morro faults). For the source of the induced stress we use the dislocation models published by Khazaradze and Klotz (2003) and Bejar-Pizarro et al. (2010) for interseismic coupling of the subduction zone and coseismic rupture of the Tocopilla earthquake, respectively. To estimate the stress imparted on the Morro and Mej receiver faults, we use the formulation of Okada (1992) in an elastic half-space with shear modulus and Poisson ratio of 3×10^{10} Pa and 0.25, respectively. The stress is calculated at about 2 km depth near the center of the fault planes obtained in the uniform slip inversion

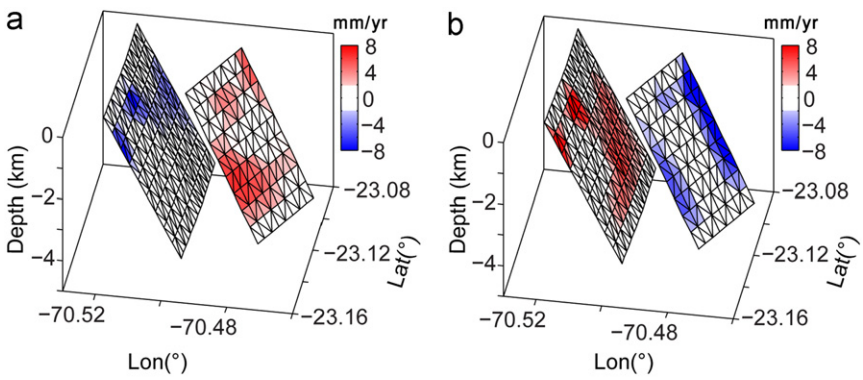

Fig. 4. Distributed slip model for (a) interseismic and (b) postseismic periods. The red color represents reverse faulting and blue associates with normal faulting. (For interpretation of the references to color in this figure legend, the reader is referred to the web version of this article.)

Table 2
Stress change due to interseismic plate coupling (using coupling model of Khazaradze and Klotz, 2003) and Tocopilla event (using slip model of Bejar-Pizarro et al., 2010) on 55° east dipping faults. Positive shear stress values encourage reverse slip and positive normal stress values indicate compression across the fault.

Period	Fault name	Shear	Normal
Interseismic (bars/yr)	Morro	−0.016	−0.003
	Mej	+0.004	−0.02
Coseismic (bars)	Morro	+0.121	+0.035
	Mej	−0.06	+0.087

for pure dip–slip faulting. Table 2 summarizes the results of the stress calculation on the Morro and Mej faults during the interseismic and coseismic periods. Here positive shear stress values encourage reverse slip and positive normal stress values indicate compression across the fault. As shown in the cross section of horizontal normal stress (see Supplementary Fig. S6 in the Appendix), the interseismic coupling model produces localized tension within a broad zone of compression near Mejillones Peninsula, which encourages an opposite sense of slip on the Morro and Mej faults despite their short distance from one another (see Supplementary Fig. S6 in the Appendix and Table 2). The Tocopilla rupture model induces a stress field that is opposite to the interseismic result (see Supplementary Fig. S6 in the Appendix) and encourages normal slip while adding compressional fault-normal stress on both faults. The Mejillones Peninsula is located at the transition zone of compressional and tensional stress, which might be poorly constrained, likely due to the inaccuracy of the simple models we use.

According to Byerlee's (1978) law, shear stress on a critically stressed fault is ~45 MPa at a depth of 2 km, where the lithostatic stress is ~53 MPa. To reverse the slip direction, stress changes of that order would be required on a frictionally strong fault. However, the amplitude of the coseismic stress change (Table 2) on the Morro and Mej faults of ~10 kPa is very small, requiring these creeping faults to be frictionally very weak to allow for the observed slip reversal. This finding is consistent with results for the shallow creeping San Andreas and Hayward strike–slip faults, where coseismic stress changes on the order of 10–50 kPa produced reversals in slip direction following the 1983 Coalinga and 1989 Loma Prieta earthquakes, respectively (Simpson et al., 1988b; Lienkaemper et al., 1997; Toda and Stein, 2002). The inference of low ambient stress is also consistent with the findings of Kato et al. (2011) and Ryder et al. (2012) who describe normal faulting earthquakes in the hanging wall of the 2011 M9 Tohoku and 2010 M8.8 Maule earthquakes in areas that experienced shortening in prior decades.

Following 1999 Hector Mine earthquake, several adjacent faults experienced retrograde motion that can be explained as an elastic response of compliant fault zones to the coseismic stress perturbations (Fialko et al., 2002). To test the hypothesis of a compliant fault zone response, we use Eqs. (2) and (4) of Fialko et al. (2002) to estimate maximum vertical and strike–slip displacements at Morro and Mej faults due to coseismic stress changes from the Tocopilla earthquake. To this end we assume a 2-km-wide fault zone, a factor of three reduction in the shear modulus relative to the surrounding rocks and a maximum shear and normal stress change of 10 kPa. These values provide us with an estimate of the maximum displacement at the fault zone. The obtained strike–slip displacement is ~1 mm and that of vertical is 0.1 mm. Given the north–south orientation of Morro and Mej faults, the equivalent LOS displacement is about 0.2 mm, thus much less than observed for the pre- and postseismic periods. Also, the elastic fault zone response is immediate, whereas we observe a prolonged postseismic displacement. Therefore, aseismic fault creep remains the best explanation for the observed deformation.

To illustrate the effect of the subduction seismic cycle on the crustal faults, which causes the local uplift/subsidence and stress perturbations we estimated above, we present a schematic view of the surface displacement induced by the plate coupling and coseismic rupture of the Tocopilla event. Fig. 5 shows the vertical displacement along a trench-perpendicular profile that passes through Mejillones. As shown in Fig. 5c and d the change in the sense of interplate displacement causes bulging (interseismic) and down-warping (co- to postseismic) of the crust resulting in a narrow zone of extension or contraction near the surface of the upper plate in the different stages of the seismic cycle (see also Savage, 1983 for discussion on this narrow zone). Thus, the changes in ambient stress induced by the megathrust earthquake cycle on the creeping faults appear to be able to change their sense of slip at least near the surface. We also note that the postseismically observed fault block uplift according to this interpretation should decline in rate over time and, gradually, shift back to the interseismic kinematic mode of local block subsidence superimposed on regional uplift as a result of increased elastic bulging.

In view of the small stress perturbations resulting from the interseismic loading and the coseismic strain release, the immediate response of the faults and their changing kinematics requires very low fault strengths and background stress levels. Our observations pertain to the upper 4 km of the crust and we suggest that the faults are likely locked below ~4 km. The behavior of the deeper, possibly seismogenic portion of the faults is unknown. There is no instrumentally recorded seismicity at mid- to lower-crustal depth in this area in the past decades, but

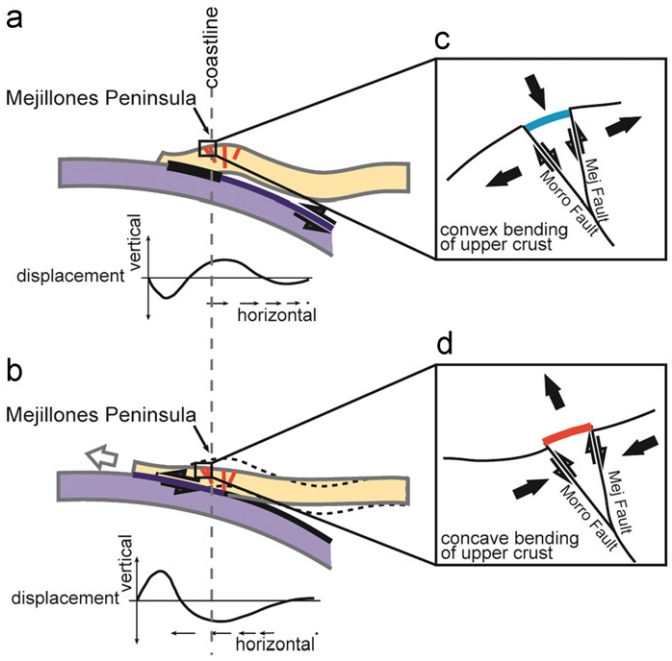

Fig. 5. Profiles showing (a) interseismic as well as (b) coseismic deformation of the forearc (modified after Chlieh et al., 2004). The location of Mejillones Peninsula and the location of the Morro and Mejillones faults are marked with a box west of the overall coastline location in N-Chile (stippled line). (c) Box shows detail of Morro and Mejillones faults during convex bending of the upper crust during the interseismic phase causing normal faulting on Morro fault and reverse faulting on Mejillones fault. (d) Box shows detail of Morro and Mejillones faults during concave bending during the coseismic and early postseismic phase causing the reversal of motion along both faults.

major creep seems to be precluded from modeling of GPS data (Khazaradze and Klotz, 2003). Hence, the observed kinematic reversal appears to be restricted to the upper crustal creeping portions of the faults with little impact on the deeper parts, which may be locked. Our observations suggest that the mode of shallow faulting activity in the crustal forearc varies through the seismic cycle of the megathrust, while the long-term deformation across the Peninsula is extensional across the slowly uplifting forearc. We suggest that changes or transients of the mode of the faulting in the forearc systems may therefore be used as an indirect proxy for assessing the state of plate convergence occurring at depth.

6. Conclusions

By using interferometric synthetic aperture radar and inverse modeling we present a rare example of two shallow crustal faults that slip aseismically and change their sense of slip due to reversal of stress conditions associated with a megathrust earthquake on the underlying plate interface. The 2007 Tocopilla earthquake changed the sense of slip on the Mej and Morro faults on the Mejillones Peninsula, opposite to that observed during preceding years of interseismic deformation. Moreover, both faults are shown to have experienced contrasting kinematics during each stage of the seismic cycle, in spite of very similar orientations. We infer from our results that the loading/unloading of the crust during the earthquake cycle of the underlying seismogenic plate interface (1) can encourage creep on weak faults in the overlying plate and govern its mechanism, (2) may cause slip reversal related to the loading cycle of the upper plate with some permanent strain accumulation, (3) and the state of stress may be inferred by monitoring the kinematic behavior of forearc faults.

Acknowledgments

We would like to thank the editor and two anonymous reviewers for their insightful comments. The interferograms used in this study were generated using the GMTSAR software (Sandwell et al., 2011). Radar data is provided by the European Space Agency under project C1P-9539.

Appendix A. Supplementary material

Supplementary data associated with this article can be found in the online version at http://dx.doi.org/10.1016/j.epsl.2012.04.001.

References

Allmendinger, R.W., Gonzalez, G., 2010. Invited review paper: neogene to quaternary tectonics of the coastal Cordillera, Northern Chile. Tectonophysics 495 (1–2), 93–110.

Armijo, R., Thiele, R., 1990. Active faulting in Northern Chile—ramp stacking and lateral decoupling along a subduction plate boundary. Earth Planet. Sci. Lett. 98 (1). 40–61.

Bejar-Pizarro, M., Carrizo, D., Socquet, A., Armijo, R., Barrientos, S., Bondoux, F., Bonvalot, S., Campos, J., Comte, D., de Chabalier, J.B., Charade, O., Delorme, A., Gabalda, G., Galetzka, J., Genrich, J., Nercessian, A., Olcay, M., Ortega, F., Ortega, I., Remy, D., Ruegg, J.C., Simons, M., Valderas, C., Vigny, C., 2010. Asperities and barriers on the seismogenic zone in North Chile: state-of-the-art after the 2007 Mw 7.7 Tocopilla earthquake inferred by GPS and InSAR data. Geophys. J. Int. 183 (1), 390–406.

Berardino, P., Fornaro, G., Lanari, R., Sansosti, E., 2002. A new algorithm for surface deformation monitoring based on small baseline differential SAR interferograms. IEEE Trans. Geosci. Remote Sensing 40 (11), 2375–2383.

Bjerhammar, A., 1973. Theory of errors and generalized matrix inverse. Elsevier publishing company, Amsterdam, pp. 127–128.

Byerlee, J.D., 1978. Friction of rocks. Pure Appl. Geophys. 116, 615–626.

Chen, C.W., Zebker, H.A., 2001. Two-dimensional phase unwrapping with use of statistical models for cost functions in nonlinear optimization. J. Opt. Soc. Am. A 18, 338–351.

Chlieh, M., de_Chabalier, J.B., Ruegg, J.C., Armijo, R., Dmowska, R., Campos, J., Feigl, K.L., 2004. Crustal deformation and fault slip during the seismic cycle in the North Chile subduction zone, from GPS and InSAR observations. Geophys. J. Int. 158 (2), 695–711.

Collettini, C., Niemeijer, A., Viti, C., Marone, C., 2009. Fault zone fabric and fault weakness. Nature 462 (7275). 907–910.

Costantini, M., Rosen, P.A., 1999. A generalized phase unwrapping approach for sparse data. In: Proceedings of the IEEE 1999 International Geoscience and Remote Sensing Symposium (IGARSS). Hamburg, pp. 267–269.

Delouis, B., Philip, H., Dorbath, L., Cisternas, A., 1998. Recent crustal deformation in the Antofagasta region (Northern Chile) and the subduction process. Geophys. J. Int. 132 (2), 302–338.

Ferretti, A., Prati, C., Rocca, F., 2001. Permanent scatterers in SAR interferometry. IEEE Trans. Geosci. Remote Sensing 39, 8–20.

Fialko, Y., 2006. Interseismic strain accumulation and the earthquake potential on the southern San Andreas fault system. Nature 441 (7096), 968–971.

Fialko, Y., Sandwell, D., Agnew, D., Simons, M., Shearer, P., Minster, B., 2002. Deformation on nearby faults induced by the 1999 Hector Mine earthquake. Science 297 (5588), 1858–1862.

Franceschetti, G., Lanari, R., 1999. Synthetic aperture radar processing. Library of Congress Cataloging-in-Publication Data.

Gonzalez, G., Cembrano, J., Carrizo, D., Macci, A., Schneider, H., 2003. The link between forearc tectonics and pliocene-quaternary deformation of the Coastal Cordillera, Northern Chile. J. S. Am. Earth Sci. 16 (5), 321–342.

Kato, A., Sakai, S., Obara, K., 2011. A normal-faulting seismic sequence triggered by the 2011 off the Pacific coast of Tohoku Earthquake: wholesale stress regime changes in the upper plate. Eur. Political Sci. 63, 745–748.

Khazaradze, G., Klotz, J., 2003. Short- and long-term effects of GPS measured crustal deformation rates along the south central Andes. J. Geophys. Res. 108 (B6). ETG 5-1–ETG 5-15.

King, G.C.P., Stein, R.S., Lin, J., 1994. Static stress changes and the triggering of earthquakes. Bull. Seism. Soc. Am. 84, 935–953.

Lienkaemper, J.J., Galehouse, J.S., Simpson, R.W., 1997. Creep response of the Hayward fault to stress changes caused by the Loma Prieta earthquake. Science 276 (5321), 2014–2016.

Lienkaemper, J.J., McFarland, F.S., Simpson, R.W., Bilham, R.G., Ponce, D.A., Boatwright, J.J., Caskey, S.J., 2012. Long-term creep rates on the Hayward Fault: Evidence for controls on the size and frequency of large earthquakes. Bull. Seismol. Soc. Am. 102 (1), 31–41.

Lin, J., Stein, R.S., 2004. Stress triggering in thrust and subduction earthquakes and stress interaction between the southern San Andreas and nearby thrust and strike–slip faults. J. Geophys. Res. 109 (B2).

Loveless, J.P., Pritchard, M.E., Kukowski, N., 2010. Testing mechanisms of subduction zone segmentation and seismogenesis with slip distributions from recent Andean earthquakes. Tectonophysics 495 (1–2), 15–33.

Marone, C., 1998. Laboratory-derived friction laws and their application to seismic faulting. Annu. Rev. Earth Planet. Sci. 26, 643–696.

Marquardt, C., Fomari, M., Lavenu, A., Vargas, G., Ortlieb, L., Ritz, J.F., Philip, H. and Marinovic, N., 2005. Volcanic ash dating from the Mejillones Peninsula (23°S): implications for the Neogene outer forearc stratigraphy, tectonics and volcanic relationships. In: Proceedings of the 6th ISAG. Barcelona, Spain.

Massonnet, D., Rossi, M., Carmona, C., Adragna, F., Peltzer, G., Feigl, K., Rabaute, T., 1993. The displacement field of the Landers earthquake mapped by radar interferometry. Nature 364, 138–142.

Meade, B.J., 2007. Algorithms for the calculation of exact displacements, strains, and stresses for triangular dislocation elements in a uniform elastic half space. Comput. Geosci. 33 (8), 1064–1075.

O'leary, D.P., 1990. Robust regression computation using iteratively reweighted least-squares. SIAM J. Matrix Anal. Appl. 11 (3), 466–480.

Okada, Y., 1985. Surface deformation due to shear and tensile faults in a half-space. Bull. Seism. Soc. Am. 75, 1135–1154.

Okada, Y., 1992. Internal deformation due to shear and tensile faults in a half-space. Bull. Seism. Soc. Am. 82, 1018–1040.

Ryder, I., Rietbrock, A., Kelson, K., Bürgmann, R., Floyd, M., Socquet, A., Vigny, C., Carrizo, D., 2012. Large extensional aftershocks in the continental forearc triggered by the 2010 Maule earthquake, Chile. Geophys. J. Int. 188 (3). 879–890.

Sandwell, D., Mellors, R., Tong, X., Wei, M., Wessel, P., 2011. Open radar interferometry software for mapping surface deformation. EOS Trans. AGU 92 (28)http://dx.doi.org/10.1029/2011EO280002.

Savage, J.C., 1983. A dislocation model of strain accumulation and release at a subduction zone. J. Geophys. Res. 88, 4984–4996.

Segall, P., Harris, R., 1987. The earthquake deformation cycle on the San Andreas fault near Parkfield, California. J. Geophys. Res. 92, 10511–10525.

Shirzaei, M., Walter, T.R., 2009. Randomly iterated search and statistical competency (RISC) as powerful inversion tools for deformation source modeling: application to volcano InSAR data. J. Geophys. Res. 114, B10401, http://dx.doi.org/10.1029/2008JB006071.

Shirzaei, M., Walter, T.R., 2011. Estimating the effect of satellite orbital error using wavelet based robust regression applied to InSAR deformation data. IEEE Trans. Geosci. Remote Sensing 49 (1), 4600–4605.

Simpson, R.W., Schulz, S.S., Dietz, L.D., Burford, R.O., 1988a. The response of creeping parts of the San-Andreas fault to earthquakes on nearby faults—2 examples. Pure Appl. Geophys. 126 (2–4), 665–685.

Simpson, R.W., Schulz, S.S., Dietz, L.D., Burford, R.O., 1988b. The response of creeping parts of the San Andreas fault to earthquakes on nearby faults: two examples. In: Stuart, W.D., Aki, K. (Eds.), Intermediate-Term Earthquake Prediction. Birkhäuser, Basel, pp. 665–685.

Stark, P.B., Parker, R.L., 1995. Bounded-variable least-squares—an algorithm and applications. Comput. Stat. 10 (2), 129–141.

Tikhonov, A.N., Arsenin, V.Y., 1977. Solutions of ill-posed problems. Scripta series in mathematics. V.H. Winston and Sons, Washington D.C.

Toda, S., Stein, R.S., 2002. Response of the San Andreas fault to the 1983 Coalinga-Nuñez earthquakes: an application of interaction-based probabilities for Parkfield. J. Geophys. Res. 107 (B6). ESE 6-1–ESE 6-16.

Victor, P., Sobiesiak, M., Glodny, J., Nielsen, S.N., Oncken, O., 2011. Long-term persistence of subduction earthquake segment boundaries: evidence from Mejillones Peninsula, Northern Chile. J. Geophys. Res.–Solid Earth, 116.

Wang, K., Hu, Y., Bevis, M., Kendrick, E., Smalley, R., Lauria, E., 2007. Crustal motion in the zone of the 1960 Chile earthquake: detangling earthquake-cycle deformation and forearc-sliver translation. Geochem. Geophys. Geosyst., 8.